Supplementary Information (SI) for ChemComm.
This journal is © The Royal Society of Chemistry 2025

Supplementary Information

Exploration of e_g orbital occupancy in Prussian blue analogues for enhanced oxygen evolution reaction

Guicheng Li, [a] Nan Jiang*[a]

a. School of chemistry and Chemical Engineering, Guizhou University,550025, Guiyang, Guizhou, China. E-mail: njiang@gzu.edu.cn

*Corresponding authors: Nan Jiang

E-mail: njiang@gzu.edu.cn

Experimental Section

Chemicals and reagents

Cobalt (II) nitrate hexahydrate ($Co(NO_3)_2·6H_2O$, ≥ 99%), Nickel (II) nitrate hexahydrate ($Ni(NO_3)_2·6H_2O$, ≥ 99 %), Iron (III) nitrate nonahydrate ($Fe(NO_3)_3·9H_2O$, ≥ 99 %) were purchased from Macklin Chemical Co., Ltd.. Potassium hexacyanoferrate (III) ($K_3[Fe(CN)_6]$, ≥ 99%) was obtained from Energy Chemical Co., Ltd.. Potassium hydroxide (KOH, ≥ 85 %), ethanol (CH_3CH_2OH, ≥ 99%), hydrochloric acid (HCl, ≈ 37%), acetone (CH_3COCH_3, ≥ 99.5 %) were brought from Chuangdong Chemical Co., Ltd.. All reagents were used without further purification. Iron, cobalt and copper foams were purchased from Suzhou Zhengrong New Materials Co., Ltd., whereas the nickel foam was obtained from Suzhou Sinero Technology Co., Ltd.. All metal foams (0.5×1.0 cm) were successively sonicated in acetone and 3.0 M HCl solution for 10 min to remove the MO_x species and organic layers on their surfaces. Subsequently, they were thoroughly rinsed with deionized (DI) water and ethanol several times. The water was deionized (< 12 MΩ) with a Haokang technology pure-water system.

Material characterizations

X-ray diffraction (XRD) patterns were obtained using a Bruker D8 Advance X-ray diffractometer equipped with Cu Kα radiation (λ = 1.5406 Å). X-ray photoelectron spectroscopy (XPS) analyses were carried out on a Thermo Scientific Nexsa apparatus with an Al Kα X-ray source (hv =1486.6 eV). The oerating voltage was 15 kV, and the working current was 10 mA. The sample was analyzed under a vacuum of $5×10^{-10}$ Pa with an energy of 50 eV for the survey scan. Electron paramagnetic resonance (EPR Bruker A300) analyses were executed to detect the oxygen vacancies of catalysts. The morphology of the samples was observed using a high-resolution transmission electron microscope (HRTEM) (JEM-F200) and a field-emission scanning electron microscope (FE-SEM, Hitachi SU8010) equipped with an energy-dispersive X-ray (EDX) spectroscopy (Bruker XFlash 6|60). The ultraviolet and visible (UV-vis) absorption spectrum was obtained by Shimadzu UV-2700 UV/vis spectrophotometer (Shimadzu Co., Japan).

Synthesis of FeCNM$_A$ PBA

The preparation of the FeCNM$_A$ PBA was achieved through three consecutive steps. The production of FeCNCo PBA is presented as an example to demonstrate the synthesis procedures. Initially, cathodic reduction was performed in 0.1 M $Co(NO_3)_2$ solution using a **BioLogic SP-150e** electrochemical workstation. In detail, a three-electrode system was assembled where a bare cobalt foam (CF) served as the working electrode, a carbon rod was used as the counter electrode, and an Ag/AgCl (saturated KCl) was employed as the reference electrode. During the cathodic reduction process, $Co(OH)_2$ nanosheets were electrodeposited onto bare CF via a potentiostatic method at −1.0 V vs. Ag/AgCl for 30 minutes.[1] The electrodeposition process of $Co(OH)_2$ can be described by the followings equations (eq1 and eq2).[2] After deposition, the resulting indigo $Co(OH)_2$/CF was rinsed with DI water. Subsequently, the derivatization was conducted using a potentiostatic approach at 0.5 V vs. Ag/AgCl for 30 minutes, with the $Co(OH)_2$/CF electrode immersed in a 0.5 mM $K_3[Fe(CN)_6]$ solution. During this process, $Co(OH)_2$ acted as a self-sacrificial template, and the $Co(OH)_2$/CF was gradually transformed to FeCNCo PBA through an in-situ reaction. The electrode was then thoroughly washed with DI water and ethanol again, then dried in a vacuum oven at 40 ℃. The obtained electrode pre-FeCNCo PBA was placed downstream in a tube furnace to ensure sufficient contact with N_2 gas stream. The furnace was heated to 200 ℃ at a rate of 5 ℃ min^{-1} under a nitrogen atmosphere and maintained for 2 hours. After naturally cooling to the room temperature, the final product, denoted as FeCNCo PBA was obtained. The synthesis of FeCNFe PBA, FeCNNi PBA, and FeCNCu PBA was performed using the similar procedures described above.

$$NO_3^- + 7H_2O + 8e^- \rightarrow NH^{4+} + 10OH^- \tag{1}$$

$$Co^{2+} + 2OH^- \rightarrow Co(OH)_2 \tag{2}$$

Electrocatalytic measurements

All electrochemical experimental data were acquired using an electrochemical workstation (**BioLogic SP-150e**) in a standard three-electrode system at room temperature. The FeCNCo PBA self-supported electrode (0.5 cm×0.5 cm) was directly employed as the working electrode. A graphite rod and an Ag/AgCl (saturated KCl) were served as the counter electrode and reference electrode, respectively. The reference electrode in aqueous media was calibrated with ferrocenecarboxylic acid whose Fe^{3+}/Fe^{2+} redox couple has a potential of 0.328 V vs. Ag/AgCl. All measured potential values are referred to the reversible hydrogen electrode (RHE), which can be calculated using the equation: $E_{RHE} = E_{Ag/AgCl} + 0.059 \times pH + 0.197$. For OER studies in 1.0 M KOH solutions, all linear sweep voltammograms (LSVs) were recorded within the potential range from 1.0 to 1.7 V vs. RHE at a scan rate of 5 mV s^{-1}, without any iR compensation. All LSV curves for OER were iR-corrected according to the following equation:

$$E_{corrected} = E_{measured} - iR_s \tag{3}$$

where $E_{corrected}$ is the iR-corrected potential, $E_{measured}$ and i are the experimentally measured potential and current, respectively, and R_s is the solution resistance.

The Tafel slope is determined from the LSV polarization curves in accordance with the Tafel equation: $\eta = b \times \log(j) + a$, where η represents the overpotential, b denotes the Tafel slope, and j is the current density. Electrochemical impedance spectroscopy (EIS) measurements were executed within a frequency ranging from 0.01 Hz to 100 kHz with an amplitude of 10 mV. The electrochemical double-layer capacitance (C_{dl}) can be calculated from the CV curves measured at various scan rates (0.4, 0.6, 0.8, 1.0, 1.2, 1.4 mV s^{-1}). The turnover frequency (TOF) was utilized to evaluate the intrinsic activity of FeCNM$_A$ PBA (M_A = Fe, Co, Ni, and Cu), which was calculated according to the following equation:

$$TOF = (I \times Z_2)/(Z \times Q_{redox}) \tag{4}$$

where I is the measured current from LSV curves, Z is the number of electrons transferred during the electrocatalytic OER, and Z_2 represents the number of electrons transferred during the metal electrocatalysis. Q_{redox} represents the redox charges of metals (peak area).[3] The long-term durability measurement was carried out by continuous chronopotentiometry at a current density of 50 mA cm^{-2} for 20 h.

DFT calculations

All the calculations were performed within the framework of density functional theory using the projector augmented plane-wave method, as implemented in the Vienna ab initio simulation package.[4] The generalized gradient approximation proposed by Perdew-Burke-Ernzerhof (PBE) was selected for the exchange-correlation potential.[5] The cut-off energy for plane wave was set to 480 eV. The energy criterion for the iterative solution of the Kohn-Sham equation was set to 10^{-4} eV. All structures were relaxed until the residual forces on the atoms decreased to less than 0.05 eV/Å. To avoid interlaminar interactions, a vacuum spacing of 20 Å was applied perpendicular to the slab.

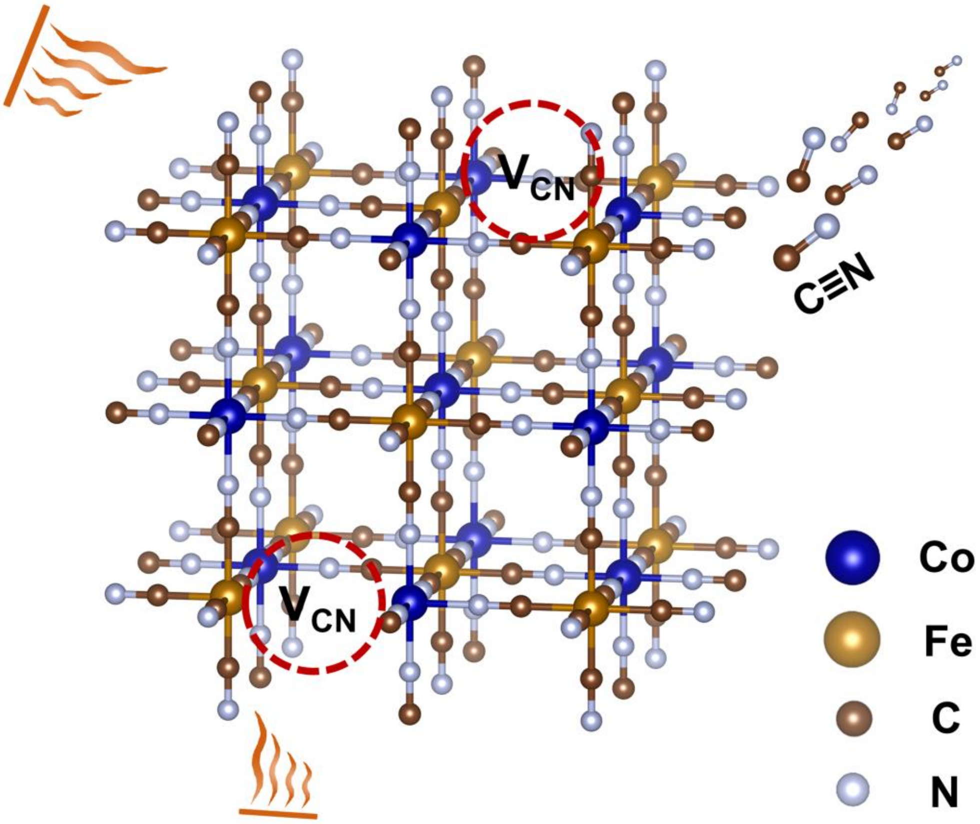

Fig. S1 Schematic illustration of the formation of V_{CN} within the FeCNCo PBA lattice through a mild thermal treatment.

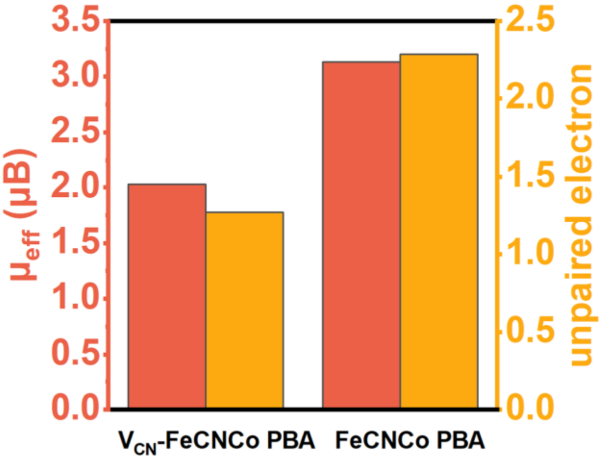

Fig. S2 Calculated the effective magnetic moments (μ_{eff}) and unpaired electrons of V_{CN}-FeCNCo PBA and FeCNCo PBA for Co site.

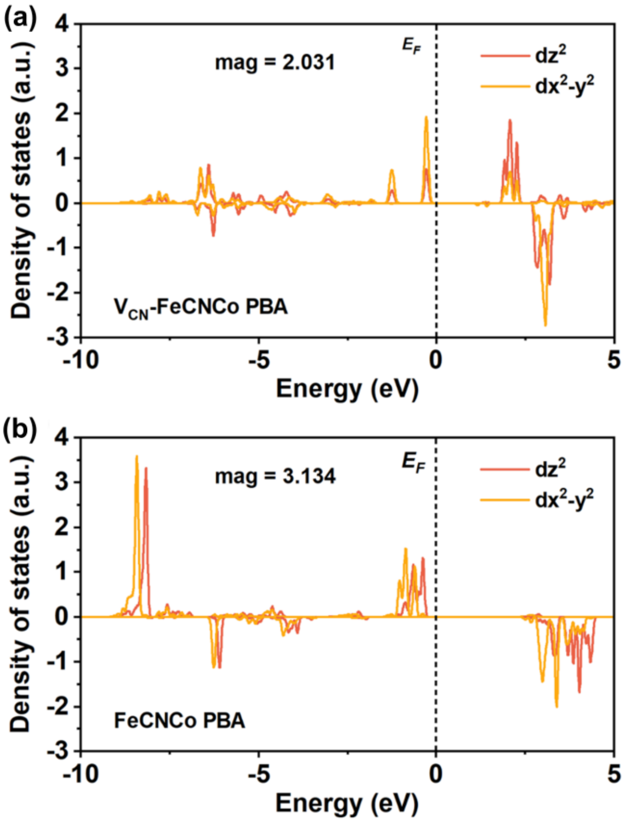

Fig. S3 Projected Co site e_g orbital density of states of (a) V_{CN}-FeCNCo PBA and (b) FeCNCo PBA.

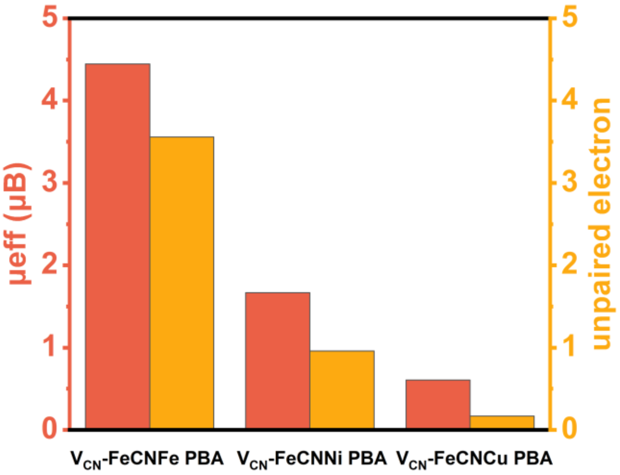

Fig. S4 Calculated the effective magnetic moments (μ_{eff}) and unpaired electrons of V_{CN}-FeCNFe PBA, V_{CN}-FeCNNi PBA, and V_{CN}-FeCNCu PBA.

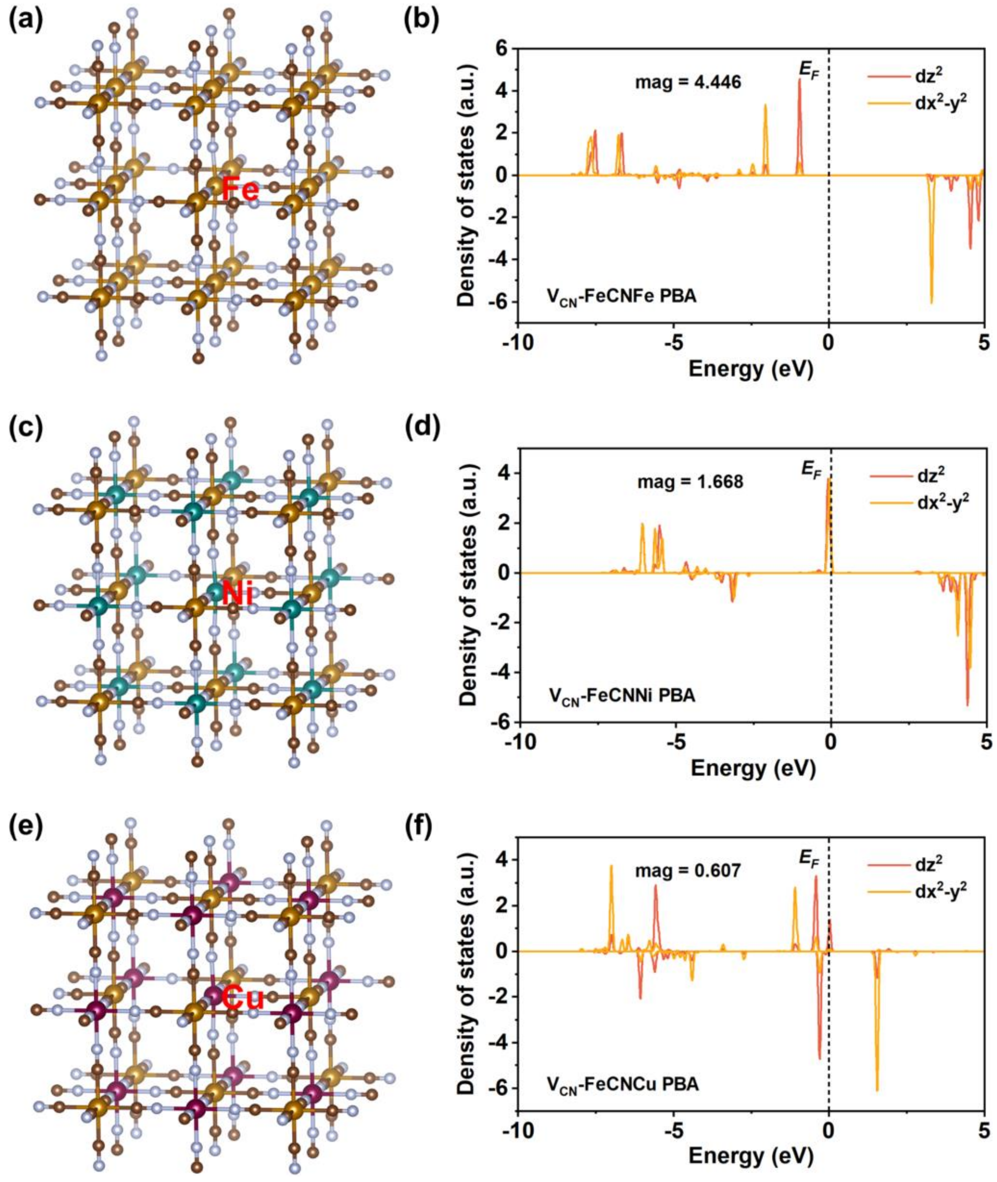

Fig. S5 Schematic illustration of (a) V$_{CN}$-FeCNFe PBA, (c) V$_{CN}$-FeCNNi PBA, and (e) V$_{CN}$-FeCNCu PBA lattice structures. Projected M$_A$ site e_g orbital density of states of (b) V$_{CN}$-FeCNFe PBA, (d) V$_{CN}$-FeCNNi PBA, and (f) V$_{CN}$-FeCNCu PBA.

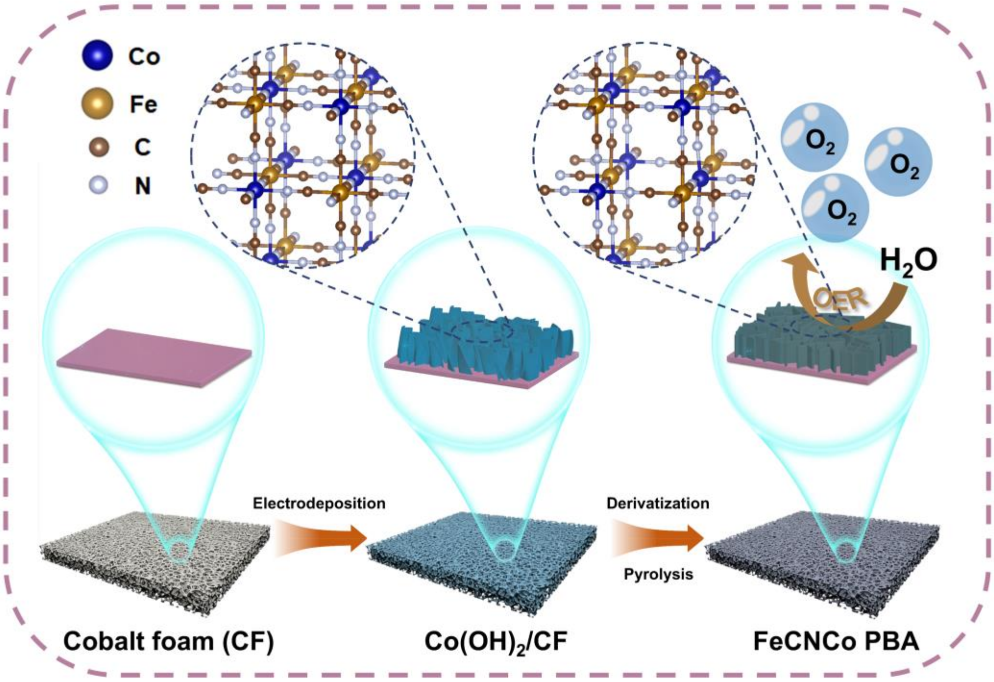

Fig. S6 Schematic illustration of the preparation process of FeCNCo PBA.

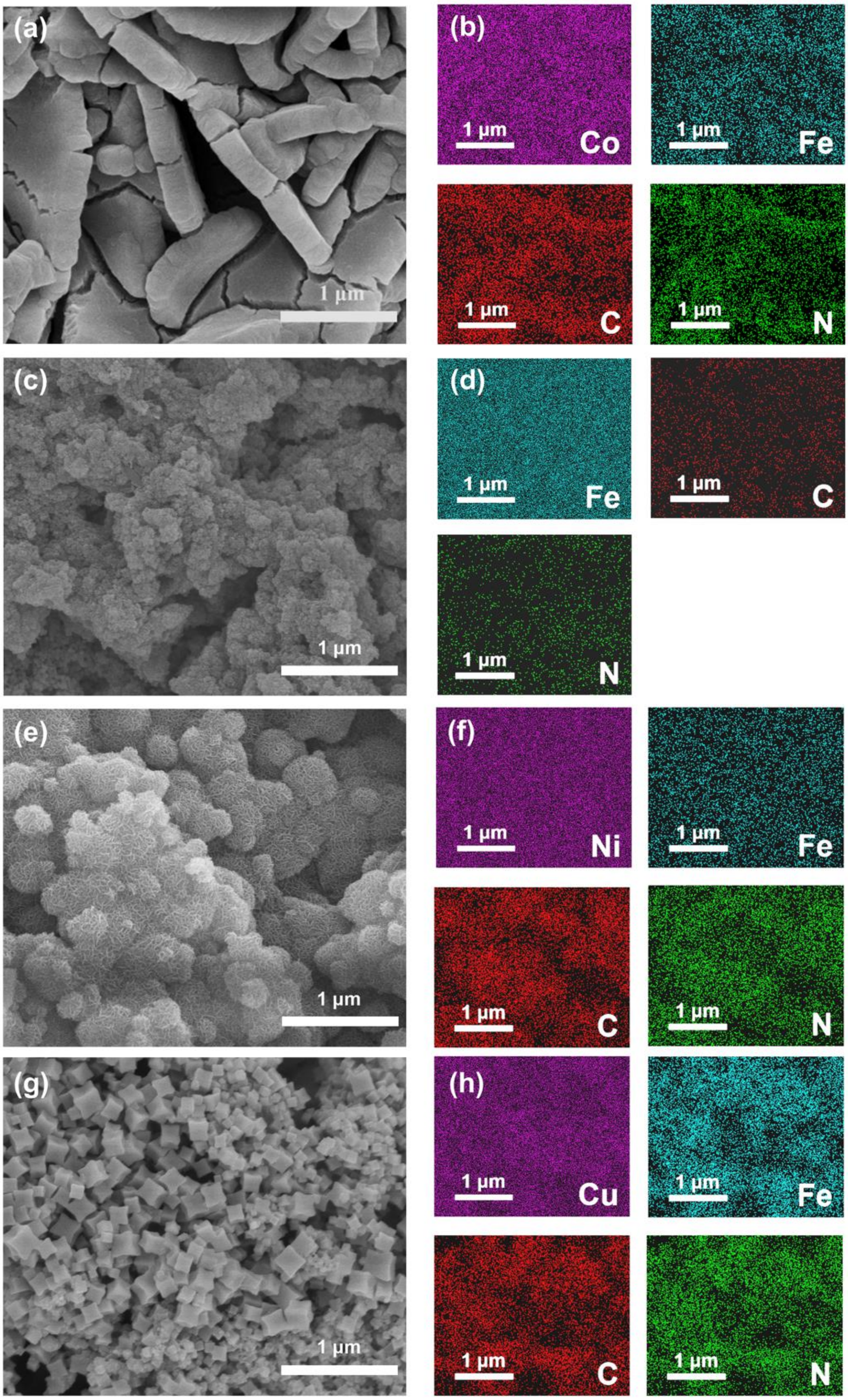

Fig. S7 SEM images of (a) FeCNCo PBA, (c) FeCNFe PBA, (e) FeCNNi PBA and (g) FeCNCu PBA. EDX element mapping images of (a) FeCNCo PBA, (c) FeCNFe PBA, (e) FeCNNi PBA and (g) FeCNCu PBA.

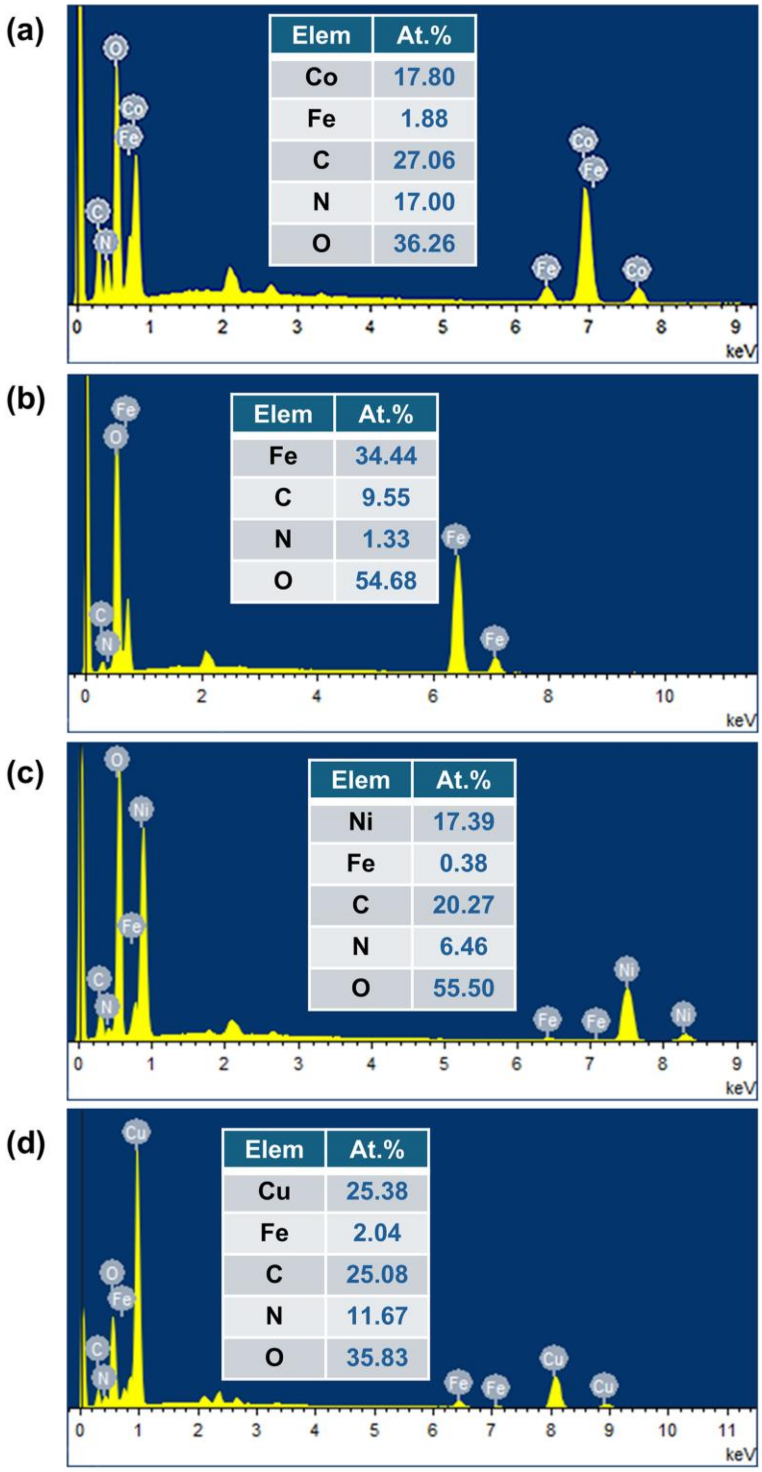

(a)

Elem	At.%
Co	17.80
Fe	1.88
C	27.06
N	17.00
O	36.26

(b)

Elem	At.%
Fe	34.44
C	9.55
N	1.33
O	54.68

(c)

Elem	At.%
Ni	17.39
Fe	0.38
C	20.27
N	6.46
O	55.50

(d)

Elem	At.%
Cu	25.38
Fe	2.04
C	25.08
N	11.67
O	35.83

Fig. S8 EDX spectra of (a) FeCNCo PBA, (b) FeCNFe PBA, (c) FeCNNi PBA and (d) FeCNCu PBA.

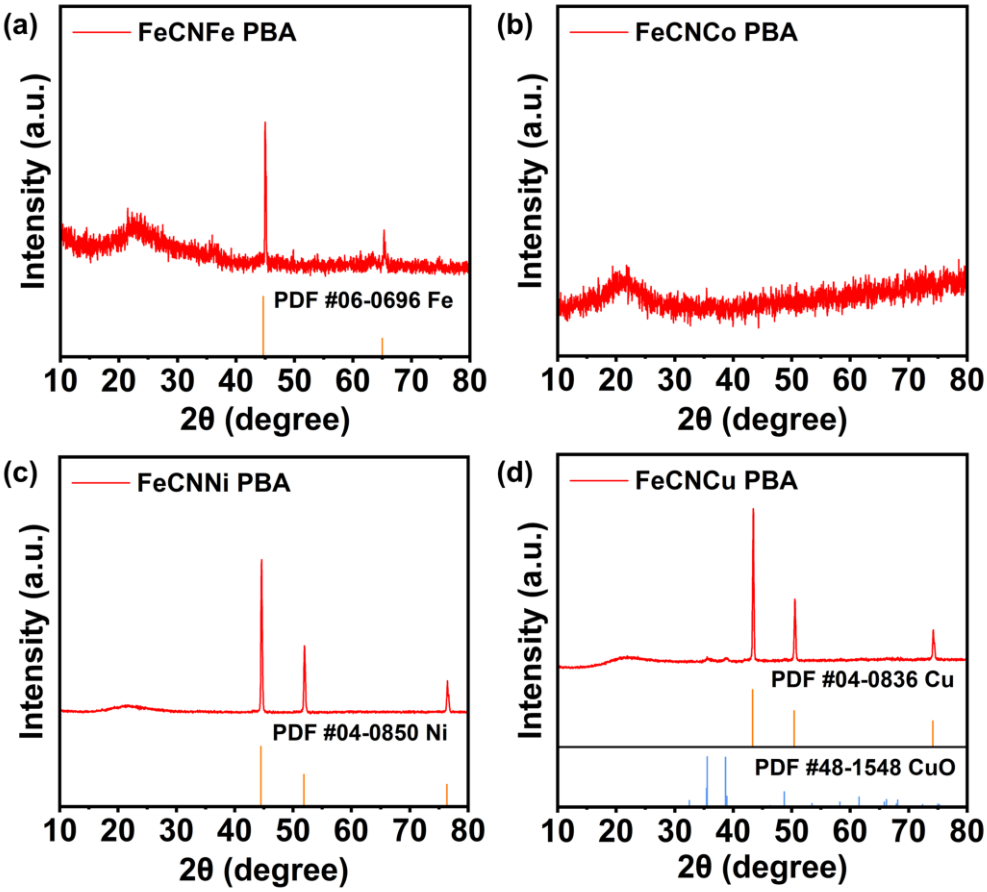

Fig. S9 XRD patterns of (a) FeCNFe PBA, (b) FeCNCo PBA, (c) FeCNNi PBA, and (d) FeCNCu PBA.

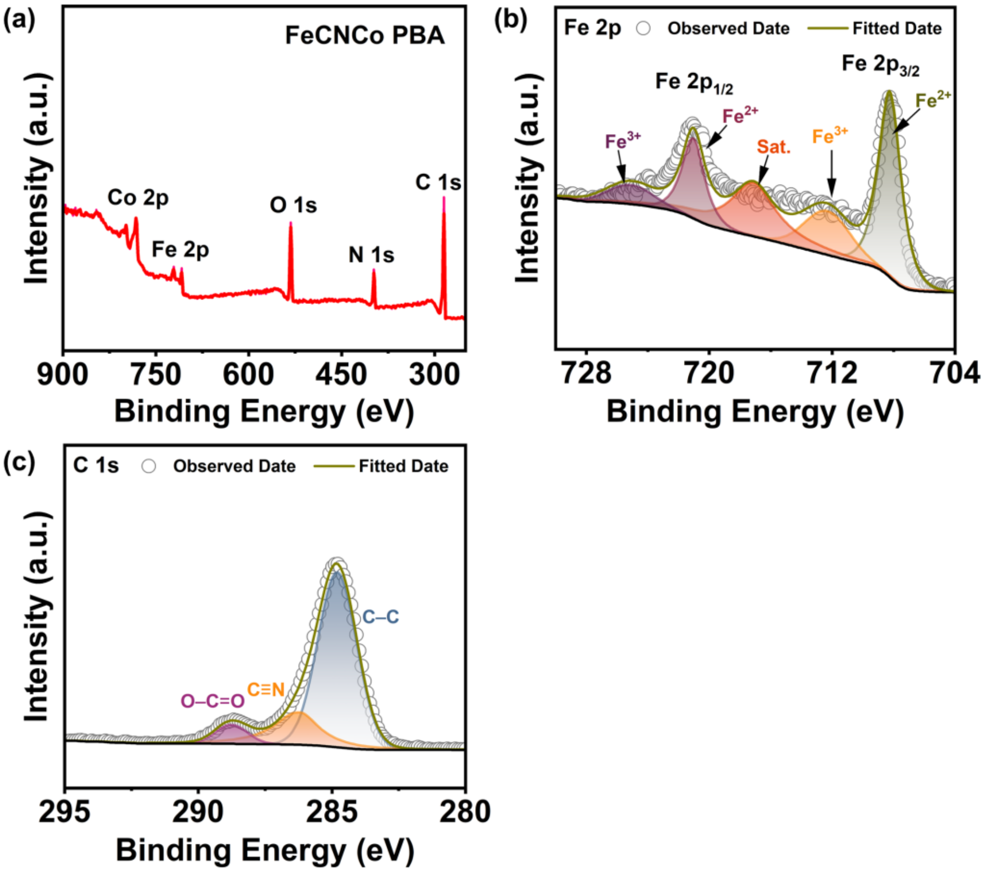

Fig. S10 (a) The XPS survey spectra of FeCNCo PBA. The high-resolution XPS spectra of (b) Fe 2p and (c) C 1s in FeCNCo PBA.

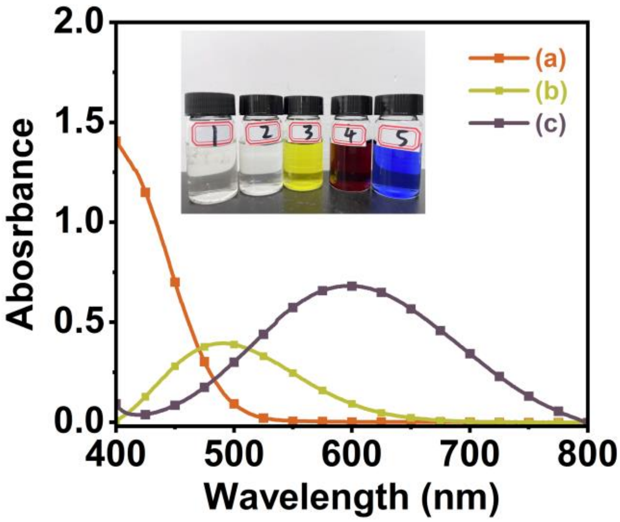

Fig. S11 Detection of cyanide in the tail gas absorbed solution by a spectrophotometer. Absorption spectra of (a) Ninhydrin + Na_2CO_3 → yellow, (b) Ninhydrin + CN + Na_2CO_3 → red and (c) Ninhydrin + CN + Na_2CO_3 + NaOH → blue. Inset: the color change of Ninhydrin solution in the presence and absence of cyanide.

Ninhydrin could be served as the color indicator according to the reported literature.[6] We utilized 0.4 wt% Ninhydrin (Sample 1 in set) to absorb the tail gas generated during the thermal treatment of FeCNCo PBA. The Ninhydrin reacts with cyanide to form colorless hydrindantin (Sample 2 in set), which reacts in the 2 wt% Na_2CO_3 solution to get a deep red-colored product (Sample 4 in set) which shows a maximum absorbance at 490 nm, and further turns to a deep blue-color product (Sample 5 in set) when adding NaOH to the red-colored solution. A strong maximum absorbance shift from 490 nm to 590 nm with increased intensity. A mixed solution of 0.4 wt% Ninhydrin and 2 wt% Na_2CO_3 exhibits yellow color (Sample 3 in set). Based on the above color changes and max absorbance changes, we can prove the formation of CN^- ions in the tail gas and V_{CN} during the pyrolysis of FeCNCo PBA.

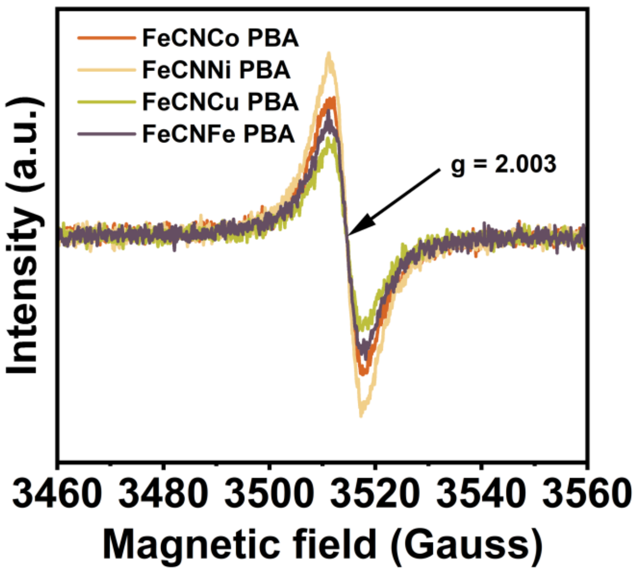

Fig. S12 EPR spectra of FeCNFe PBA, FeCNCo PBA, FeCNNi PBA, and FeCNCu PBA.

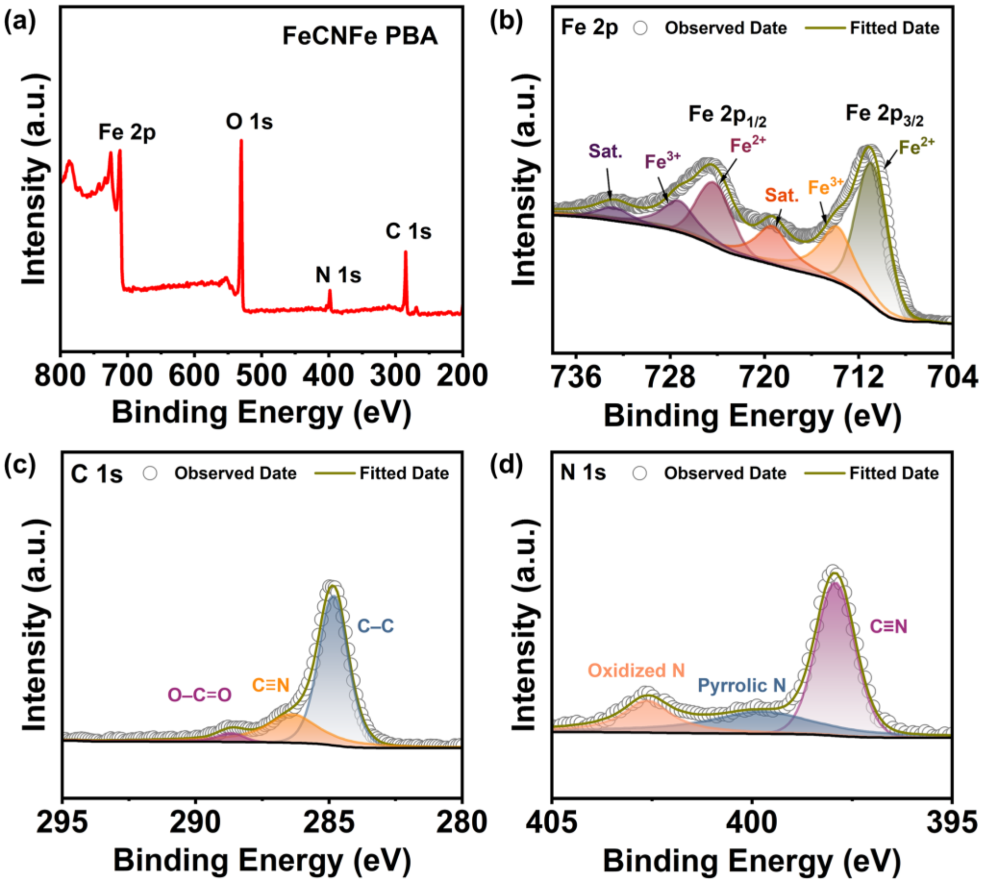

Fig. S13 (a) The XPS survey spectra of FeCNFe PBA. The high-resolution XPS spectra of (b) Fe 2p, (c) C 1s, and (d) N 1s in FeCNFe PBA.

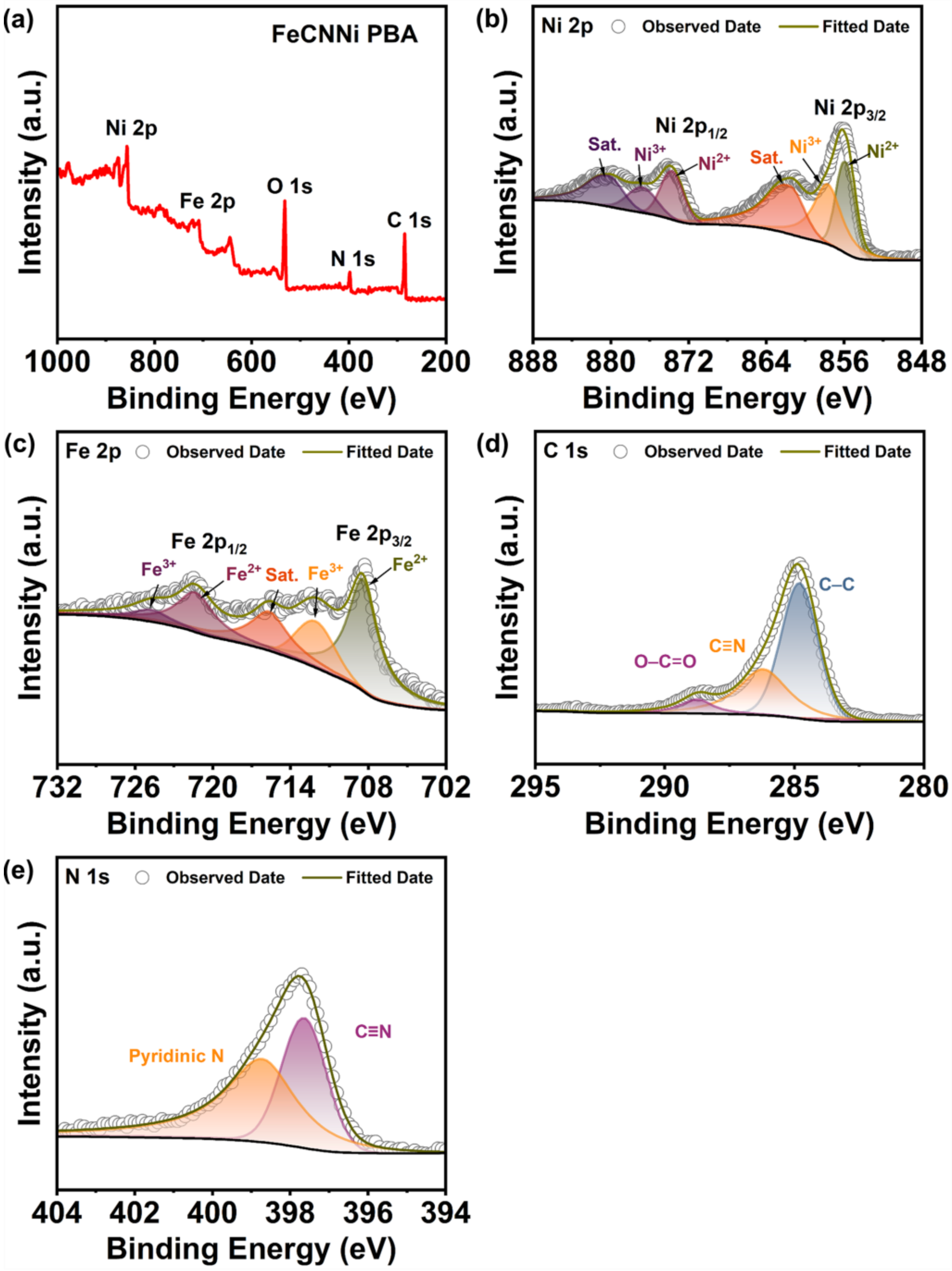

Fig. S14 (a) The XPS survey spectra of FeCNNi PBA. The high-resolution XPS spectra of (b) Ni 2p, (c) Fe 2p, (d) C 1s, and (e) N 1s in FeCNNi PBA.

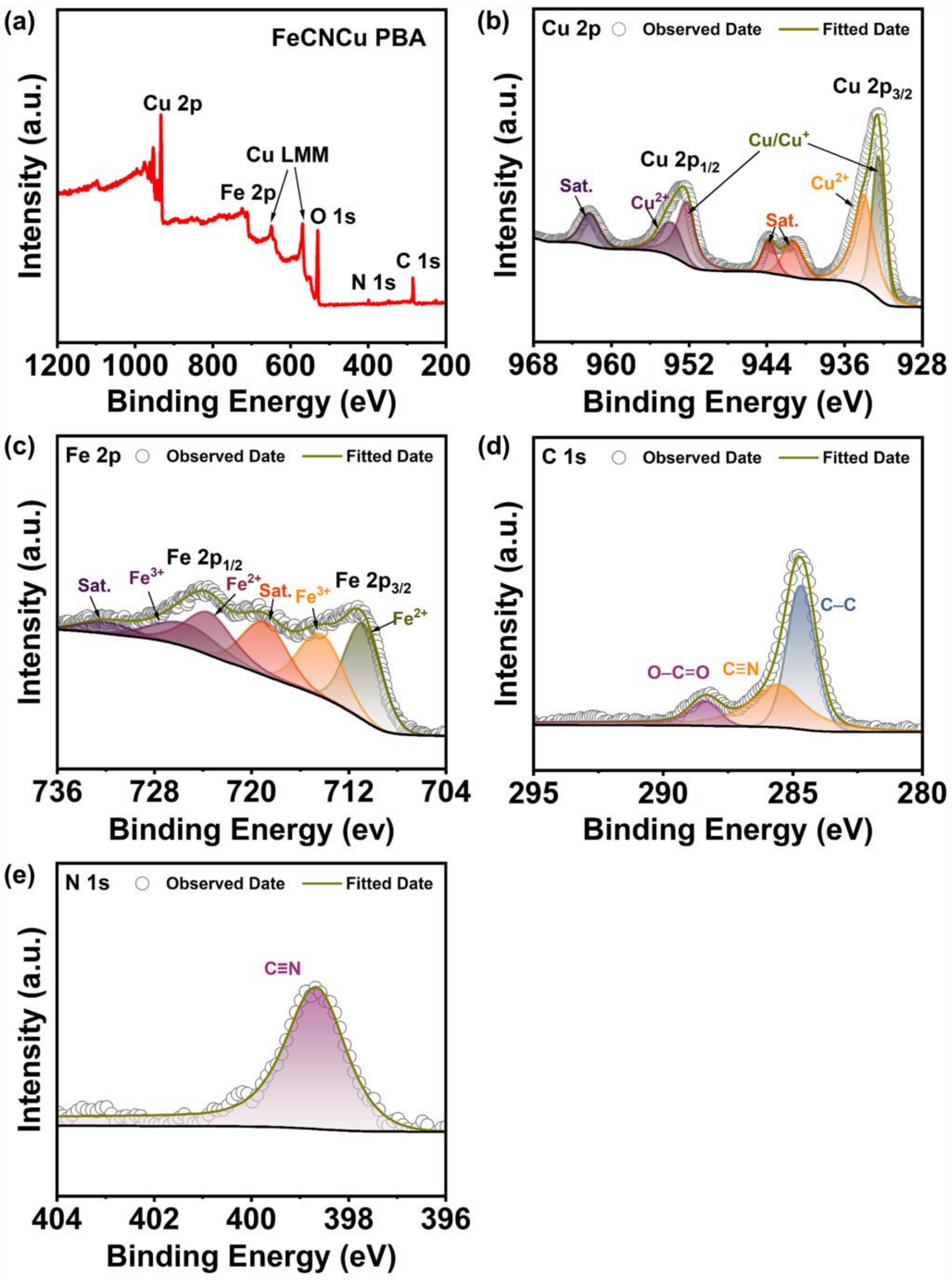

Fig. S15 (a) The XPS survey spectra of FeCNCu PBA. The high-resolution XPS spectra of (b) Cu 2p, (c) Fe 2p, (d) C 1s, and (e) N 1s in FeCNCu PBA.

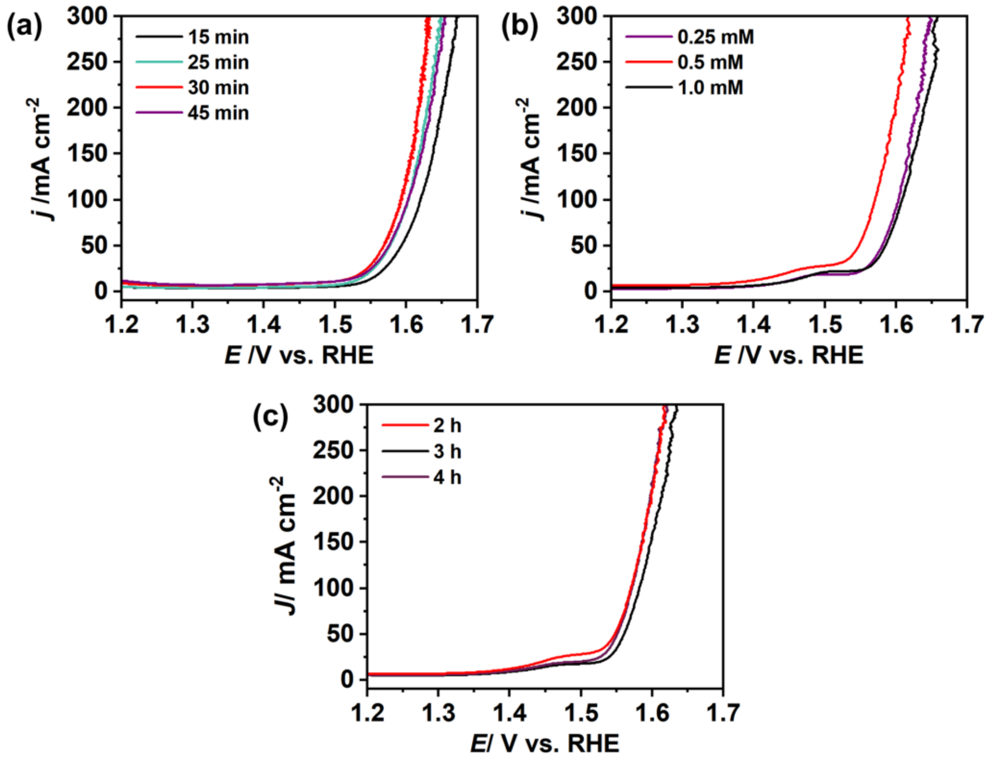

Fig. S16 (a) OER polarization curves of FeCNCo PBA prepared with different electrodeposition and derivatization times. (b) OER polarization curves of FeCNCo PBA prepared with different concentrations of $K_3[Fe(CN)_6]$. (c) OER polarization curves of FeCNCo PBA prepared with different pyrolysis times. All experiments were carried out in 1.0 M KOH.

We co-regulated the electrodeposition/derivatization durations, the concentration of $K_3[Fe(CN)_6]$, and pyrolysis temperature to optimize the electrocatalytic performance of FeCNCo PBA for OER. As shown in Fig. S16, the optimal OER activity was attained when the electrodeposition and derivatization times were 30 min, the concentration of $K_3[Fe(CN)_6]$ was 0.5 mM, and the pyrolysis time was 2 h. Therefore, the catalyst for all electrochemical tests were prepared under these optimal conditions.

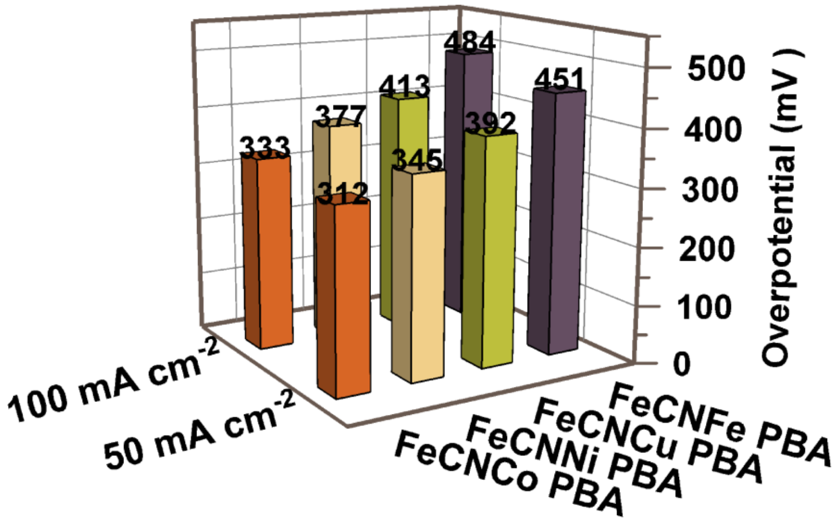

Fig. S17 Comparison of the overpotentials of four PBAs at current densities of 50 and 100 mA cm^{-2}.

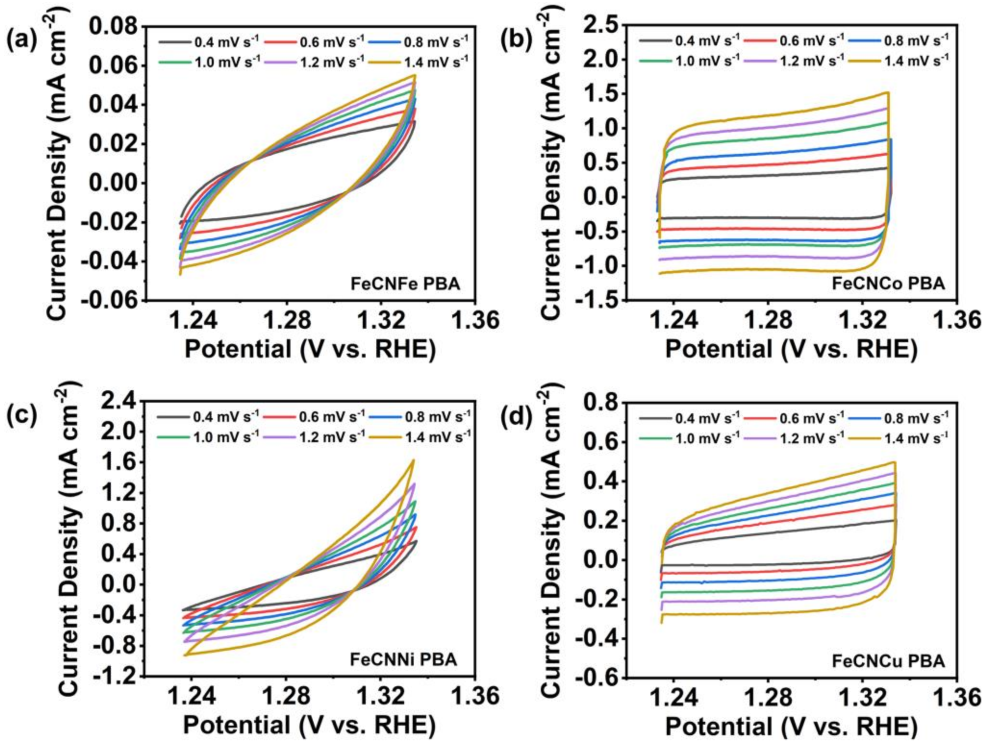

Fig. S18 The CV curves within a non-faradaic reaction region ranging from 1.23 to 1.33 V vs. RHE at different scan rates for (a) FeCNFe PBA, (b) FeCNCo PBA, (c) FeCNNi PBA, and (d) FeCNCu PBA in 1.0 M KOH solution.

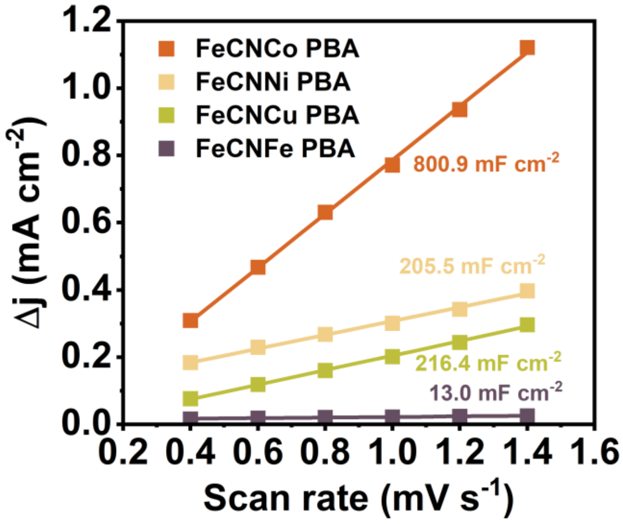

Fig. S19 Linear slopes plotted from the CVs of four PBAs at different scan rates.

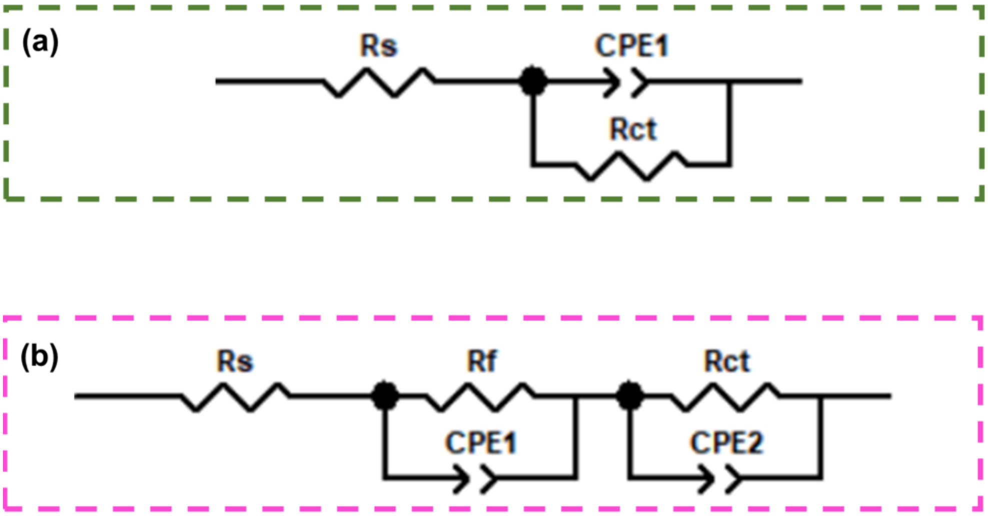

Fig. S20 (a) The equivalent circuit model of FeCNCo PBA and FeCNCu PBA. (b) The equivalent circuit model of FeCNFe PBA and FeCNNi PBA.

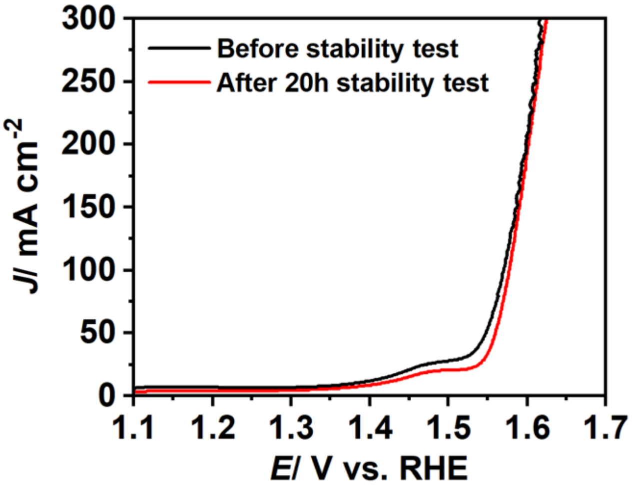

Fig. S21 Polarization curves for FeCNCo PBA before and after 20 h stability testing.

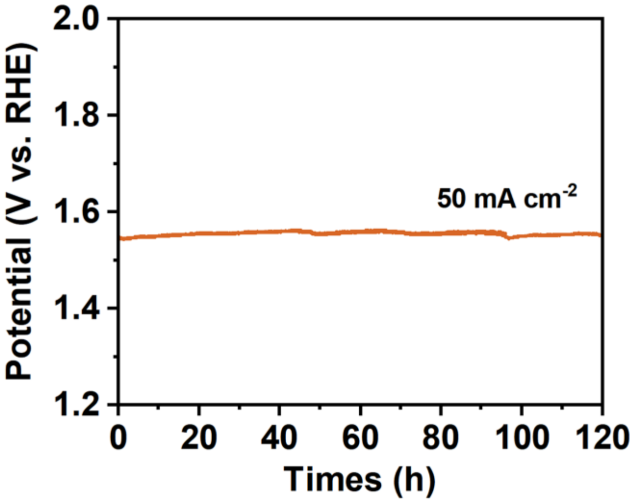

Fig. S22 Chronopotentiometry curve of FeCNCo PBA at 50 mA cm^{-2} in 1.0 M KOH solution.

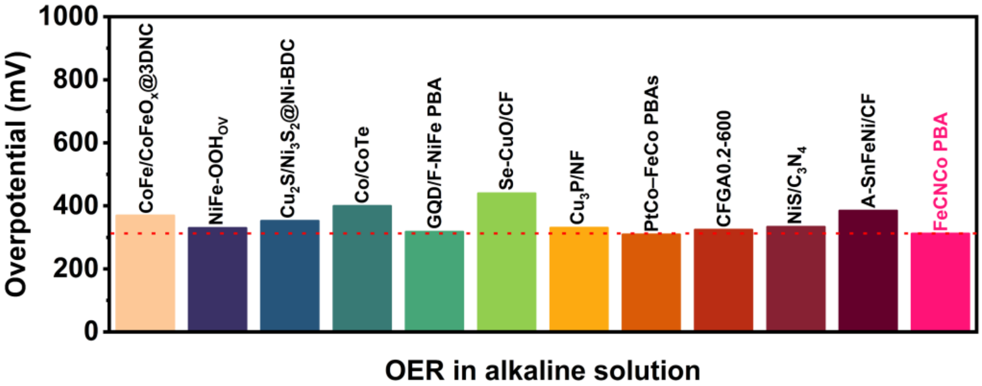

Fig. S23 Comparison of the overpotential required to drive a current density of 50 mA cm^{-2} for the FeCNCo PBA and recently reported nonprecious electrocatalysts.[7–17]

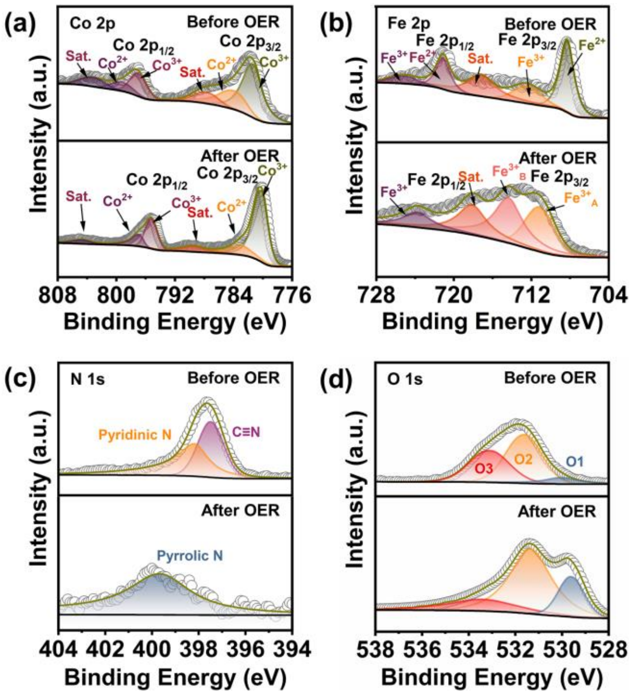

Fig. S24 XPS spectra of (a) Co 2p, (b) Fe 2p, (c) N 1s, and (d) O 1s for FeCNCo PBA after 20 h stability testing.

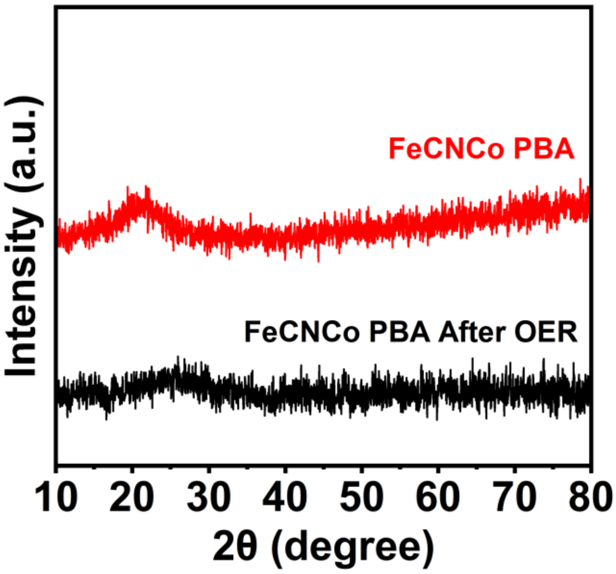

Fig. S25 XRD pattern of FeCNCo PBA after 20 h stability testing.

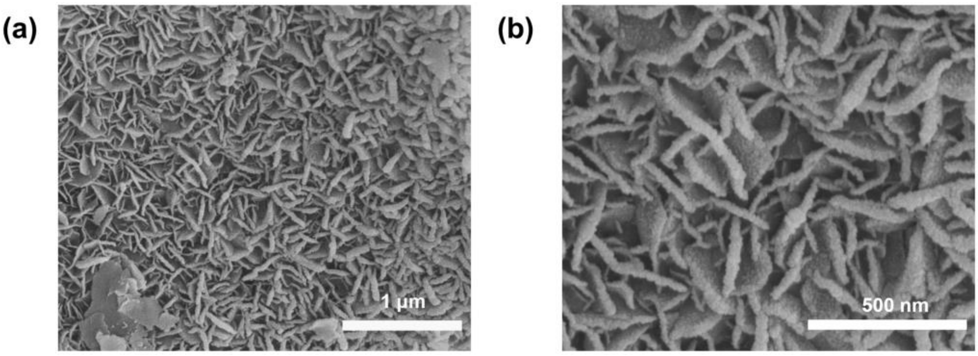

Fig. S26 SEM images of FeCNCo PBA after 20 h stability testing.

Table S1. The surface atomic ratio Fe/Co and N/Co in FeCNCo PBA obtained from XPS.

Catalysts	**Fe/Co**	**N/Co**	**V_{CN} content**
pre-FeCNCo PBA	0.69	2.43	0%
FeCNCo PBA	0.66	2.24	7.8%

Due to the large deviation of the C content measured by XPS, the C/Fe content ration of sample is inaccurate. Consequently, we employed the N/Co atomic ratio to determine the relative V_{CN} contents.

Table S2. Detail information of EIS fitting values.

Sample	**FeCNCo PBA**	**FeCNNi PBA**	**FeCNCu PBA**	**FeCNFe PBA**
Element	**Value**			
R_s (Ω)	2.29	2.48	2.76	2.27
R_f (Ω)	\	0.5846	\	2.52
R_{ct} (Ω)	1.36	1.29	4.22	8.38
CPE1-T (F/cm^2)	0.33233	0.13653	0.22224	0.01225
CPE1-P (F/cm^2)	0.599213	0.38857	0.71859	0.4621
CPE2-T (F/cm^2)	\	0.25578	\	0.0038576
CPE2-P (F/cm^2)	\	0.85489	\	0.81811

Table S3. Comparison of electrocatalytic OER activity of various nonprecious catalysts in 1.0 M KOH electrolyte.

Electrocatalysts	**Current Density (mA cm^{-2})**	**Overpotential (mV)**	**Tafel slope (mV dec^{-1})**	**Reference**
FeCNCo PBA	**50** **100**	**312** **333**	**74.5**	**This work**
CoFe/CoFeO$_x$@3DNC	50	370	50.5	S1
NiFe-OOH$_{OV}$	50	330	38	S2
Cu_2S/Ni_3S_2@Ni-BDC	50	353	75	S3
Co/CoTe	50	400	94.1	S4
GQD/F-NiFe PBA	50	318	34.7	S5
Se-CuO/CF	50	440	21	S6
Cu_3P/NF	50	331	67	S7
PtCo–FeCo PBAs	10	310	41.3	S8
CFGA0.2-600	10	325	63.02	S9
NiS/C_3N_4	10	334	45	S10
A-SnFeNi/CF	100	385	103	S11

Table S4. Comparison of O 1s spectrum in FeCNCo PBA before OER and after OER.

FeCNCo PBA	**Metal–oxygen (O1) at%**	**Hydroxyl species (O2) at%**	**Absorbed water (O3) at%**
Before OER	9.02	52.34	38.64
After OER	21.17	60.40	18.43

Reference

1 L. Quan, S. Li, Z. Zhao, J. Liu, Y. Ran, J. Cui, W. Lin, X. Yu, L. Wang, Y. Zhang and J. Ye, *Small Methods*, 2021, **5**, 2100125–2100134.

2 X.-F. Wang, Z. You and D.-B. Ruan, *Chinese Journal of Chemistry*, 2006, **24**, 1126–1132.

3 S. Anantharaj, P. E. Karthik and S. Noda, *Angew Chem Int Ed*, 2021, **60**, 23051–23067.

4 G. Kresse and D. Joubert, *Phys. Rev. B*, 1999, **59**, 1758–1775.

5 J. P. Perdew, K. Burke and M. Ernzerhof, *Phys. Rev. Lett.*, 1996, **77**, 3865–3868.

6 P. Nagaraja, M. S. Hemantha Kumar, H. S. Yathirajan and J. S. Prakash, *ANAL. SCI.*, 2002, **18**, 1027–1030.

7 M. Hou, S. Gong, L. Ji, J. Huang, M. Xu and Z. Chen, *Chemical Engineering Journal*, 2021, **419**, 129575–129585.

8 Z. Ahmed, Krishankant, R. Rai, R. Kumar, T. Maruyama, C. Bera and V. Bagchi, *ACS Appl. Mater. Interfaces*, 2021, **13**, 55281–55291.

9 R. Jiang, Y. Cheng, T. Wang, Y. Zhu, C. Cao, X. Ma, G. Liu and L. Chen, *International Journal of Hydrogen Energy*, 2024, **49**, 647–657.

10 R. Yoo, K. Min, H. Kim, D. Lim and S.-H. Baeck, *Applied Surface Science*, 2022, **581**, 152405–152412.

11 A. M. Tarigan, S. Aulia, M. Rinawati, L.-Y. Chang, Y.-S. Cheng, C.-C. Chang, W.-H. Huang, J.-L. Chen, H. Setyawan and M.-H. Yeh, *Chemical Engineering Journal*, 2023, **476**, 146754–146764.

12 L. Tabassum, H. Tasnim, S. Shubhashish, I. Perera, T. Bhosale, M. Li, S. March, M. K. Islam and S. L. Suib, *Applied Materials Today*, 2022, **27**, 101485–101494.

13 Z. Yang, Y. Tuo, Q. Lu, C. Chen, M. Liu, B. Liu, X. Duan, Y. Zhou and J. Zhang, *Green Energy & Environment*, 2022, **7**, 236–245.

14 C. Zeng, Q. Li, Y. You, L. Sun, W. Cheng, X. Zheng, S. Liu and Q. Wang, *International Journal of Hydrogen Energy*, 2022, **47**, 35149–35155.

15 L. Liu, H. Huang, J. Tai, X. Wu, Z. Guo, X. Shen, S. Cui and X. Chen, *Carbon*, 2024, **219**, 118847–118859.

16 Y. Luo, J. Qin, G. Yang, S. Luo, Z. Zhao, M. Chen and J. Ma, *Chemical Engineering Journal*, 2021, **410**, 128394–128404.

17 S. Li, R. Ma, Y. Lu, Y. Pei, M. Yang, J. Wang and D. Liu, *J. Mater. Chem. A*, 2020, **8**, 5919–5926.